



Sputter-Deposited Pt/CrN Nanoparticle PEM Fuel Cell Cathodes: Limited Proton Conductivity Through Electrode Dewetting

M. D. Gasda, G. A. Eisman,* and D. Gall^z

Department of Materials Science and Engineering, Rensselaer Polytechnic Institute, Troy, New York 12180, USA

Platinum-coated chromium nitride electrodes are deposited onto gas diffusion layers by normal and glancing angle deposition and are tested as cathodes for proton exchange membrane (PEM) fuel cells. X-ray diffraction and scanning electron microscopy show that the CrN forms 111-oriented nanoparticles with {100} facets that are covered by 3.4×10^{11} Pt mounds/cm², independent of Pt loading 0.05 to 0.25 mg/cm². Polarization curves exhibit $dE/d(\log i)$ slopes $b \approx -100$ and -150 mV/dec for high ($E > 0.75$ V) and low ($E < 0.5$ V) potentials, respectively, but show an anomalous drop with $b \approx -420$ mV/dec in the intermediate voltage range. This is attributed to poor proton conduction associated with a reversible dewetting of electrode pores during low current operation. Quantitative analyses of rate-dependent polarization curves and electrochemical impedance spectra show that the time scale for pore filling by process water is 10^3 s, and that the ionic resistance R_C within the electrode increases by a factor of 4, from $R_C \approx 0.2$ to $0.8 \Omega \text{ cm}^2$, as E increases from 0.5 to 0.8 V. The increasing electrode resistance is attributed to a low water production rate at low current, which allows the relatively hydrophobic CrN to expel water from the electrode pores, resulting in a higher resistance for ionic transport. These results show that even ultrathin sputtered catalyst layers can exhibit incomplete flooding.

© 2009 The Electrochemical Society. [DOI: 10.1149/1.3247351] All rights reserved.

Manuscript submitted June 26, 2009; revised manuscript received September 17, 2009. Published November 13, 2009.

Proton exchange membrane (PEM) fuel cells hold much promise for portable and automotive applications due to their high conversion efficiency and power density.¹ One obstacle to the widespread commercialization of fuel cells is the high cost of the platinum catalyst. Therefore, much effort is devoted to replacing or reducing the Pt loading w .² Most of today's commercial fuel cells minimize w by using a network of 30–50 nm wide carbon particles that support 2–5 nm wide Pt nanoparticles.^{3,4} A challenge associated with this Pt/C approach is a decreasing efficiency and limited lifetime due to sintering and growth of the Pt,⁵ peroxide attack of the membrane,⁶ and carbon corrosion.⁷ Moreover, some reports suggest that the lower limit in reducing Pt loading in this approach has already been reached, as reducing w to below 0.40 and 0.05 mg/cm² for cathode and anode, respectively, decreases the output efficiency.^{8,9} Considerable efforts have been directed at replacing the precious metal catalyst with other less costly materials. One possible material is CrN, which has a lower activity than Pt,¹⁰ but is an attractive candidate to supplement or replace Pt in lower cost fuel cell electrodes because of its well-known wear and corrosion resistance.¹¹ Industrial CrN coatings are most commonly deposited by reactive magnetron sputtering. Sputter deposition has also gained interest for Pt catalyst deposition,^{2,12–17} as it provides a pathway to fabricate very low Pt loading ($w = 0.005$ mg/cm²)¹⁸ electrodes with a high degree of control and reproducibility. We have recently reported that sputtering Pt from highly oblique incidence results in vertically oriented nanoparticles with increased mass-transport performance compared with continuous layers sputtered from normal incidence.¹⁹ This approach is based on the glancing angle deposition (GLAD) technique,²⁰ which exploits atomic shadowing effects during line-of-sight physical vapor deposition to engineer nanorods into various shapes, such as nanopillars,^{21–24} zigzags,^{25,26} nanospirals,²⁷ nanotubes,²⁸ two-component rods,^{29–31} and branched nanocolumns,^{32–34} with such potential applications as photonic crystals,²⁷ sensors,²⁶ catalyst supports,^{35,36} magnetic storage media,³⁷ radiation-resistant coatings,³⁸ and field emitters.³⁹

As compared with conventional Pt/C catalyst layers, higher Pt utilization is expected for ultrathin (< 500 nm)⁴⁰ sputtered catalyst layers because the electrode is flooded with water and it is therefore possible for the entire exposed surface area of Pt to be in electrolytic

contact with the membrane.⁴¹ No ionomer or other proton-conducting phase is added to ultrathin sputtered catalyst layers. In the absence of ionomer, however, water within the electrode represents the primary proton conduction path. This is in stark contrast to conventional ionomer-bonded Pt/C electrodes where the low proton conductivity of water is negligible. In fact, water flooding is not desired in conventional electrodes because it suppresses oxygen transport and leads to associated mass-transport losses. However, oxygen transport within ultrathin layer electrodes is generally adequate. Thus, increasing the water-filled volume fraction has a negligible effect on oxygen transport but actually enhances the overall performance by facilitating proton transport to all parts of the electrode.⁴⁰ The classical concept of a three-phase interface is replaced for ultrathin electrodes by a two-phase interface of electronically conductive Pt saturated with water that is in intimate contact with the membrane. The electrode is saturated with water, which transmits protons to the catalyst, and oxygen diffuses a short distance through this water to catalyst sites. Although it is recognized that the amount of liquid water within the electrode must be a function of the applied current density,⁴² it is generally assumed that the electrode is always completely filled with liquid water. This can be attributed to hydrophilic Pt, which has a reported contact angle with water of zero.⁴³ However, we expect two-phase electrodes that employ nonmetallic hydrophobic materials to exhibit incomplete flooding, and the fraction of the pores that are filled with water is likely a function of operating conditions, particularly the current density, which directly correlates to water production. The reported water contact angle for sputter-deposited CrN ranges from 80 to 100° at room temperature^{44,45} and 79–88° at 70°C.⁴⁶ Consequently, we expect thin-film electrodes that contain CrN to exhibit incomplete flooding, which in turn affects proton transport and ultimately fuel cell performance. Therefore, it is important to develop a quantitative understanding of how operating conditions affect pore flooding and proton transport in CrN containing electrodes.

In this paper, we report on Pt/CrN PEM fuel cell electrodes where the Pt is sputter-deposited on vertically oriented CrN nanoparticles grown by GLAD on the gas diffusion layer (GDL). With this model system, we show that water produced by the CrN-supported electrode can change the proton conductivity of the catalyst layer and the current density generated for a given electrode potential. At high potential, the hydrophobic CrN rejects sufficient water to result in a decrease in proton conductivity within the electrode, which in turn results in a suppressed output current in an intermediate potential range of $0.5 \text{ V} < E < 0.75 \text{ V}$. The current

* Electrochemical Society Active Member.

^z E-mail: galld@rpi.edu

increases sharply for decreasing $E < 0.5$ V as the electrode pores fill with product water, providing proton conduction to all parts of the electrode. Polarization curves at different scan rates and directions demonstrate that the water buildup and removal are completely reversible with a time constant in both cases on the order of 10^3 s, and electrochemical impedance spectroscopy (EIS) shows that the cause of the overpotential is well-modeled as ionic resistance within the catalyst layer. These results demonstrate that the assumption that water fills the entire two-phase catalyst layer is invalid for the Pt/CrN materials system, and consequently that the design of thin-film electrodes that involve hydrophobic materials requires consideration of proton conduction throughout the electrode by controlled water management.

Experimental

CrN layers were deposited directly on the microporous layer (MPL) of commercially available GDL substrates (Sigracet 35BC supplied by SGL Technologies, GmbH). The MPL is a Teflon-bonded layer of carbon nanoparticles through which reactants and products diffuse, and it provides electrical and thermal contact as well as mechanical support for the electrode. GDL substrates ($3.5 \text{ cm} \times 3.5 \text{ cm}$, later cut down to 10 cm^2 square electrodes) were placed in a load-locked magnetron sputter deposition system with a base pressure of $< 5 \times 10^{-8}$ Torr and heated in vacuum at 300°C for 1 h. Sputtering was done at 300°C in 3.0 mTorr 99.999% pure N_2 using a constant dc power of 350 W applied to a 5.1 cm diameter 99.95% chromium target. The Cr target was oriented such that the substrate and target surfaces were orthogonal and positioned 10 cm from the substrate, with the plane of the substrate surface intercepting the target center, as described in more detail in Ref. 29. Due to the finite size of the target, this arrangement leads to an average deposition angle of $\alpha = 85^\circ$. Substrates were continuously rotated at 40 rpm (0.67 Hz) to facilitate the formation of vertically oriented CrN nanoparticles. The growth rate of CrN nanorods grown under the same conditions on a flat Si substrate was measured to be 4.1 nm/min, corresponding to CrN loading rates of $2.4 \mu\text{g}/(\text{cm}^2 \text{ min})$ assuming a density⁴⁷ of $5.9 \text{ g}/\text{cm}^3$ and a porosity of 50%.⁴⁸ The CrN growth time for all electrodes was 120 min, corresponding to a nominal electrode thickness of $0.5 \mu\text{m}$. The samples were coated with Pt in the same deposition system by magnetron sputtering at room temperature in 3.0 mTorr 99.999% pure Ar. A dc power of 50 W was applied to a 5.1 cm diameter 99.99% Pt target at 11 cm from the substrate with $\alpha = 0^\circ$, yielding a deposition rate of $33 \mu\text{g}/(\text{cm}^2 \text{ min})$ or $15 \text{ nm}/\text{min}$ as determined by differential weighing of samples up to 4 mg in an electronic semi-microbalance (Sartorius 2024 MP6, standard deviation $\pm 0.02 \text{ mg}$).

The Pt-coated CrN electrodes were integrated into fuel cells with 10 cm^2 active area. The anode electrodes were commercially available Pt/C with Pt loading $w = 0.25 \text{ mg}/\text{cm}^2$ (E-TEK LT120EWALTSI). The membranes were Nafion NRE-212 (Ion Power), activated by boiling in $0.5 \text{ M H}_2\text{SO}_4$ followed by three separate 30 min boiling steps in deionized water, and stored in deionized water until assembly into a fuel cell. The electrodes were bonded to the membrane at 126°C and 350 psi (2.4 MPa) for 5 min. Fuel cells were operated at 70°C with atmospheric pressure reactants humidified to a dew point of 70°C (100% relative humidity). Either air or oxygen was fed to the cathode, with a stoichiometric ratio of $\lambda = 2.5$ for $1.0 \text{ A}/\text{cm}^2$ (416 sccm) for air or $\lambda = 1.2$ for $2.0 \text{ A}/\text{cm}^2$ (84 sccm) for oxygen. Pure hydrogen was fed to the anode, with $\lambda = 1.2$ for $1.0 \text{ A}/\text{cm}^2$ (84 sccm) for air or $\lambda = 1.2$ for $2.0 \text{ A}/\text{cm}^2$ (167 sccm) for oxygen operation. Before characterization, the cells were "incubated" at 0.4 V for at least 24 h or until the output current stabilized. Polarization curves, EIS, and cyclic voltammetry were performed with a potentiostat (Parstat 2273, Princeton Applied Research). The polarization curves were obtained using a scan rate of $1 \text{ mV}/\text{s}$ in the downward (decreasing voltage) direction, corrected for ohmic resistance by extracting the average high frequency intercept of the real axis of EIS spectra measured at 0.8, 0.5,

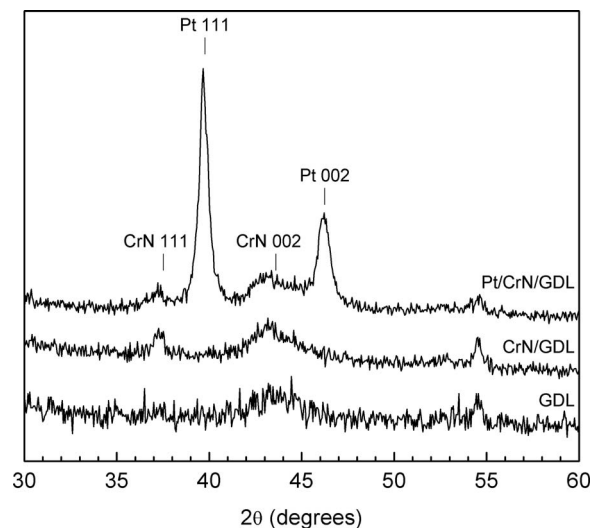


Figure 1. Grazing incidence XRD scans of uncoated GDL substrate (bottom), the GDL coated with $0.29 \text{ mg}/\text{cm}^2$ CrN (middle), and the GDL with $0.29 \text{ mg}/\text{cm}^2$ CrN coated with $0.25 \text{ mg}/\text{cm}^2$ Pt (top).

and 0.2 V, and corrected for crossover and shorting currents as described in Ref. 19. Polarization curves as a function of scan rate from 0.1 to $50 \text{ mV}/\text{s}$ were obtained in both the upward and downward directions after stabilization for 60 min at 0.8 and 0.2 V, respectively. The rate-dependent curves were not corrected for ohmic (iR) losses. The EIS was performed under steady-state conditions at cell voltages, with no iR correction applied, of $E = 0.20\text{--}0.85 \text{ V}$, using a sinusoidal voltage perturbation from 10 kHz to 0.1 Hz with a root-mean-square amplitude of 10 mV. Each EIS spectrum was analyzed by modulus-weighted least-squares fitting to an open-circuit terminus transmission line circuit model (DX type 6) using the commercial software package ZView (Scribner Associates). To converge to a continuum model, the number of reaction elements n in the model was increased until all fitting parameters became unaffected by further increases in n . This was reached with $n = 100$, which is consistent with what Makharia et al. have previously reported.⁴⁹ X-ray diffraction (XRD) measurements were done using a Bruker D8 Discover system with parallel $\text{Cu K}\alpha$ radiation from grazing incidence ($\theta = 5^\circ$). Scanning electron microscopy (SEM) was performed on a Carl Zeiss Supra 55 in secondary electron mode at 5 kV accelerating voltage.

Results and Discussion

Figure 1 shows typical grazing incidence XRD scans over a 2θ range from 30 to 60° for a GDL substrate, a CrN layer on a GDL substrate, and a complete Pt/CrN/GDL electrode with $w = 0.25 \text{ mg}/\text{cm}^2$ Pt. The bottom scan from the raw substrate exhibits a broad feature at 43.6° and a peak at 54.5° , which are associated with weak reflections from semicrystalline carbon, Teflon, and other (proprietary) materials. The second spectrum, from a GDL substrate coated with $0.29 \text{ mg}/\text{cm}^2$ of CrN, shows the same substrate reflections as the bottom scan, and one additional peak at 37.3° , associated with CrN 111, which has an expected 2θ value of 37.516° .⁵⁰ This spectrum does not permit detection of a possible CrN 002 peak, which would be expected at 43.594° and therefore overlaps with the broad substrate feature. It also cannot exclude a possible minor contribution from a mixed-in second hexagonal close-packed Cr_2N phase, with 111- and 110-reflections at 42.611 and 37.350° , respectively.⁵⁰ The top spectrum from the electrode including GDL substrate, CrN support, and Pt catalyst contains all previously discussed features plus strong reflections at 39.7 and 46.2° , associated with Pt 111 and 002.⁵⁰

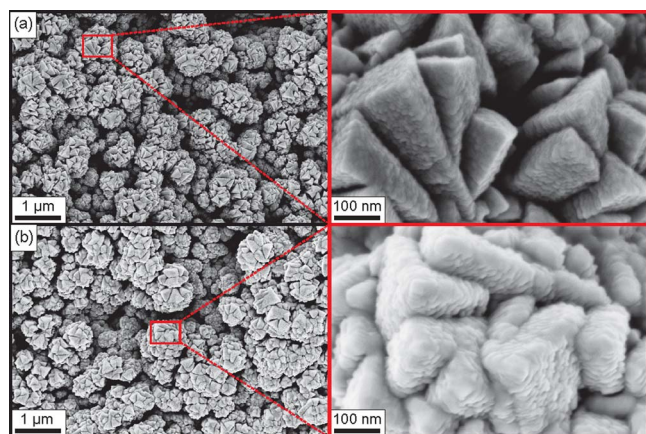


Figure 2. (Color online) Plan-view SEM micrographs showing GDL substrates that were successively coated with 0.29 mg/cm^2 CrN and (a) 0.05 and (b) 0.25 mg/cm^2 Pt.

Figure 2 shows plan-view SEM micrographs of the Pt/CrN/GDL electrodes, where 0.29 mg/cm^2 CrN was coated with 0.05 and 0.25 mg/cm^2 Pt for (a) and (b), respectively. The two samples show a similar large-scale morphology, associated with the GDL substrate that exhibits roughness features and pores in the $1\text{--}5 \text{ }\mu\text{m}$ length scale. The CrN support forms faceted grains, $100\text{--}200 \text{ nm}$ wide, as clearly observed in the high magnification image on the right in Fig. 2a. The facets are orthogonal low energy CrN{100} surfaces,⁵¹ which terminate the CrN grains to form pointed tops that protrude out of the sample surface, indicating a preferred 111-orientation. This is consistent with reported 111-textures for polycrystalline cubic transition metal nitride layers grown at low ion-bombardment conditions^{52,53} and also confirms our XRD observations, discussed above, that these samples are primarily cubic CrN, with no or negligible Cr₂N. The high magnification image in Fig. 2a also indicates that the nominally 23 nm thick Pt coating develops discrete 10 nm wide Pt mounds on the CrN{100} facets. The mound density is $3.4 \times 10^3 \text{ }\mu\text{m}^{-2}$, as determined from statistical analyses from 10 different facets. The micrograph in Fig. 2b, from an electrode with a 5 times higher Pt loading $w = 0.25 \text{ mg/cm}^2$, exhibits a comparable Pt-mound structure on the CrN facets. The mounds have, within the experimental uncertainty of 10%, the same areal number density as those in Fig. 2a, but are taller, resulting in a higher surface roughness and a correspondingly higher overall Pt surface, leading to an increase in output current as presented below.

Figure 3 shows polarization curves for three fuel cells containing Pt/CrN cathode electrodes with 0.29 mg/cm^2 CrN and Pt loadings of $w = 0.05, 0.15,$ and 0.25 mg/cm^2 . The solid lines are the E vs i curves for the cathode exposed to air, showing a voltage drop with increasing current, which is typical for PEM fuel cells and is associated with activation polarization at high potential and concentration polarization at low potential.⁵⁴ Comparing the three curves, i increases with w both in the high potential ($\sim 0.8 \text{ V}$) kinetic regime and the diffusion-controlled regime below approximately 0.5 V . At $E = 0.80 \text{ V}$, i increases from 4.7 to 8.5 to 11 mA/cm^2 for $w = 0.05, 0.15,$ and 0.25 mg/cm^2 , respectively. This increase is attributed to the increasing Pt surface area because, as noted above, increasing w leads to an increase in the Pt-mound size with a constant mound area density, resulting in an overall larger number of active surface sites. This trend is most pronounced at low Pt loading, where increasing w from 0.05 to 0.15 mg/cm^2 leads to an 80% increase in i , while further raising w to 0.25 mg/cm^2 increases i at 0.80 V by less than 25%. In contrast, in the mass-transport regime, the increase in i with w is relatively small. For example, at 0.5 V , i increases by 19 and 18% from 172 to 204 to 240 mA/cm^2 for $w = 0.05, 0.15,$

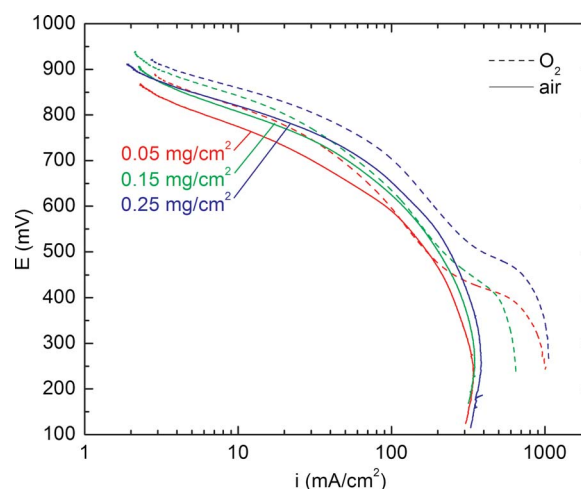


Figure 3. (Color online) Polarization curves of sputter-deposited Pt/CrN electrodes with 0.29 mg/cm^2 CrN and three different Pt loadings of $0.05, 0.15,$ and 0.25 mg/cm^2 operated with pure H₂ fuel and air (solid lines) or pure oxygen (dashed lines) as oxidant.

and 0.25 mg/cm^2 , respectively. We attribute these only small relative increases in the mass-transport regime to the nearly constant electrode morphology. Based on Fig. 2, the porosity is controlled by the structure of the GDL substrate and the CrN support layer, which are independent of w . Therefore, the low potential current, which is primarily limited by O₂ diffusion to the active sites, remains nearly unaffected by the fivefold increase in Pt loading.

The dashed lines in Fig. 3 correspond to polarization curves from the same cells, but with pure O₂ as the oxidant. The plots exhibit a logarithmic decrease in potential (dropping from 0.9 to 0.8 V) between 0 and 30 mA/cm^2 , which is qualitatively comparable to the drop (from 0.9 to 0.7 V) seen for the same cells from 0 to 40 A/cm^2 with air at the cathode. The $dE/d(\log i)$ slopes b , which are referred to as Tafel slopes in this activation regime, are $-117, -105,$ and -93 mV/dec for $w = 0.05, 0.15,$ and 0.25 mg/cm^2 , respectively, which is typical for PEM fuel cells with a Pt catalyst.⁴¹ The voltage increase at constant current associated with replacing air with oxygen, also referred to as the “O₂ gain,” is $43, 35,$ and 39 mV at 10 mA/cm^2 for $w = 0.05, 0.15,$ and 0.25 mg/cm^2 , respectively. These values are larger than 23 mV , the expected O₂ gain in the thermodynamic limit associated with the higher Nernst potential conferred by the higher partial pressure of O₂. The additional gain is attributed to a reduction of the concentration overpotential, which is small but not negligible even at low current density. In the mass-transport-limited regime below 0.4 V , the maximum output current density increases by up to 3 times when replacing air with oxygen. This relatively strong effect is primarily attributed to pores in the electrode where oxygen diffusion within air is restricted, leading to nitrogen-filled (oxygen-depleted) inactive regions and a correspondingly lower current with air as the oxidant. At intermediate potentials between 0.5 and 0.75 V , however, the absolute magnitude of b increases by about a factor of 4, and the oxygen gain is small. For example, at 150 mA/cm^2 , b is $-434, -440,$ and -401 mV/dec and the O₂ gain is $-4, +2,$ and $+46 \text{ mV}$ for $w = 0.05, 0.15,$ and 0.25 mg/cm^2 , respectively. Below 0.5 V , the magnitude of b decreases again to $-115, -242,$ and -150 mV/dec before the mass-transport-limited current is reached at $0.57, 0.44,$ and 0.65 A/cm^2 , respectively. In summary, we observe a polarization curve for operation with pure O₂ in which b quadruples at intermediate potential, with a subsequent shelf appearing at lower potential in which b rapidly decreases, before the curve finally drops off again at the limiting current density. Such behavior cannot be explained by purely structural arguments because the oxygen gain is expected to be at least the thermodynamic minimum of 23 mV for all i , and must

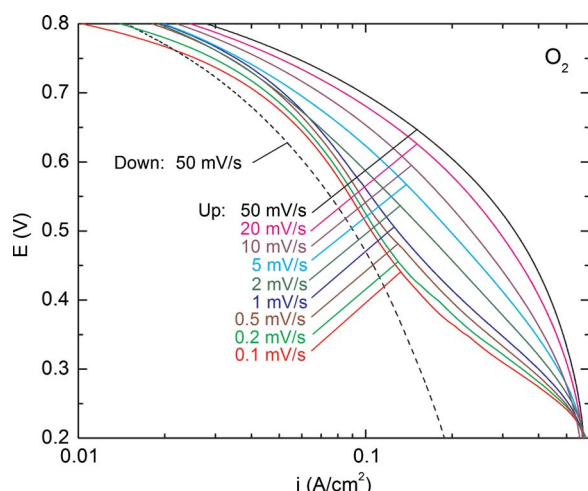


Figure 4. (Color online) Polarization curves for upward (increasing E) scans after 1 h stabilization at 0.2 V with scan rates ranging from 0.1 to 50 mV/s as labeled, from a Pt/CrN electrode with $w = 0.25$ mg/cm² Pt operated in O₂. The dashed curve is a corresponding downward (decreasing E) curve with 50 mV/s after 1 h stabilization at 0.8 V.

increase monotonically with i , as the additional concentration overpotential due to air monotonically increases with i . That is, these results suggest that a physical or chemical property of the catalyst layer changes with potential. We propose that reversible water filling of electrode pores is primarily responsible for the anomalous polarization curves shown in Fig. 3. This is discussed in detail below, after the presentation of scan-rate-dependent polarization curves and EIS results that strongly support this finding.

Figure 4 is a set of polarization curves with no iR correction applied, obtained with different upward (increasing voltage) scan rates ranging from 0.1 to 50 mV/s, from a fuel cell with $w = 0.25$ mg/cm² operated with pure O₂. Before each scan, the cell was operated at a constant 0.2 V for 1 h, yielding a reproducible current of 0.57 A/cm², indicating that transient currents are negligible after the 1 h stabilization and the cell is therefore at steady state. The polarization curves show a strong dependence on scan rate. At a high rate of 50 mV/s, the absolute slope $|dE/d(\log i)|$ in the semilogarithmic plot monotonically increases with i , which is commonly observed for PEM fuel cells⁵⁴ and is attributed to an increasing mass-transport limitation. However, as the scan rate is lowered, i is reduced for any constant E -value and the slope develops a pronounced maximum at an intermediate potential range of 0.4 V < E < 0.7 V. As the scan rate approaches zero, the curves converge for $E > 0.4$ V onto the dashed line, which is the measured polarization curve for a fast 50 mV/s scan in the downward direction after stabilizing for 1 h at 0.8 V. A slow (0.1 mV/s) downward scan yields a polarization curve (not shown) that is identical to that for the slow upward scan, indicating that the 0.1 mV/s curve represents the cell at steady state for all E .

We attribute the scan-rate dependence of the polarization curve to the filling of electrode pores by product water with a characteristic time on the order of 10³ s. Water in PEM fuel cells is known to facilitate proton transport from the membrane to reaction sites via migration under an electric field as well as diffusion.^{41,55-57} Water-filled pores conduct protons to catalyst sites that are inaccessible in the “dry” electrode. At a low potential of $E = 0.2$ V, the current and therefore the water production is high, yielding a wetted electrode with water-filled pores. Increasing E reduces the water production and therefore favors the drying of the electrode, which in turn reduces the proton conductivity. This dewetting is facilitated by CrN, which is hydrophobic in comparison to Pt,⁴³⁻⁴⁶ and sheds enough water to empty electrode pores to the degree that ionic contact to some parts of the catalyst is lost under low water production condi-

tions. We use the term “drying” here in a relative sense, not intended to mean completely dry because the reactants are fully humidified and some water is still being produced. During the fast upward scan, the electrode remains relatively well wetted, leading to a large i for a given E . Lowering the scan rate allows the pores increasingly more time for drying during the scan. Therefore, i decreases with decreasing upward scan rate, as observed in Fig. 4. In the limit of infinitely high scan rate (disregarding double-layer charging and other transient effects), the upward curve represents a maximum current density available on a wetted (ionically conductive) catalyst surface, and similarly, an infinitely fast downward scan represents a minimum current density available to a “fully dried” electrode, where fully dried refers to the level of dewetting achieved by steady-state operation at 0.8 V. In a separate experiment, hydrogen was fed to the anode and nitrogen to the cathode, and the potential was scanned to determine the contribution of capacitive charging current. The current reached a maximum of 2.1 mA/cm² at 40 mV/s, which is 2–3 orders of magnitude smaller than the oxygen reduction reaction current and therefore makes a negligible contribution to the observed scan-rate dependence. We also do not believe that this scan-rate dependence can be attributed to the reduction of a surface oxide that results in an increase in output current below a threshold voltage because the scan-rate-dependent polarization curves (Fig. 4) resume for $E < 0.5$ V, the original, high potential slope b within a factor of 1–2, indicating an electrode that gradually fills with water and sees an increase in proton conductivity with increased current. It is expected that a suddenly reduced oxide would yield a distinctly different discontinuous stepwise increase in i .

In contrast, when operating the cells with air (rather than oxygen), the polarization curves from 0.80 to 0.20 V are nearly unaffected by the scan rate. That is, rates ranging from 0.1 to 50 mV/s for both upward and downward scans (not shown) yield the same steady-state polarization curves as those presented in Fig. 3. These curves exhibit no shelf where the magnitude of b suddenly decreases at some intermediate potential $E \approx 0.5$ V. We attribute this to limited oxygen mass transport, which is the dominant contribution to the overpotential for low potential operation in air. That is, i is limited by oxygen diffusion to the reaction sites and does not increase, even though (as shown below) the proton conductivity increases with decreasing potential. The mass-transport overpotential is much larger than that caused by the poor proton conductivity, and therefore the enhancement of the proton conductivity caused by water-filled pores is offset by the decreased oxygen diffusion through these same water-filled pores. This results in the small or negative oxygen gain observed in Fig. 3, which we attribute to the different pore filling rates for different polarization curves. For a downward scan, if the cell spends more or less time in a drying mode at open-circuit voltage, the amount of water present in the electrode, and the corresponding location in E of the step change from dry to filled pores, could change substantially, resulting in some cases in a seemingly low or even negative oxygen gain. The polarization curves in air (Fig. 3) exhibit a current maximum at $E = 0.2$ V, which we attribute to the reduction of oxygen transport as pores within the electrode fill with water during the measurement scan with decreasing E . In contrast, the curves for O₂ show no peak in i but a monotonically increasing i with decreasing E because oxygen partial pressure within the pores is much higher. When scanning in the upward direction, no peak i is observed on air or O₂ because the pores are filled at the beginning of the scan and deplete with increasing E .

Figure 5 is a plot of the catalyst layer resistance R_C vs potential, from a Pt/CrN electrode cell with $w = 0.15$ mg/cm², operated with air and oxygen. These data are obtained from EIS spectra that were each fitted over the entire measured frequency range from 0.1 to 10 kHz, using a transmission line model, which describes the catalyst layer as discrete RC reaction site elements separated by series resistances corresponding to the sum of ionic and electronic resistances within the catalyst layer,^{49,58} where the electronic resistance is as-

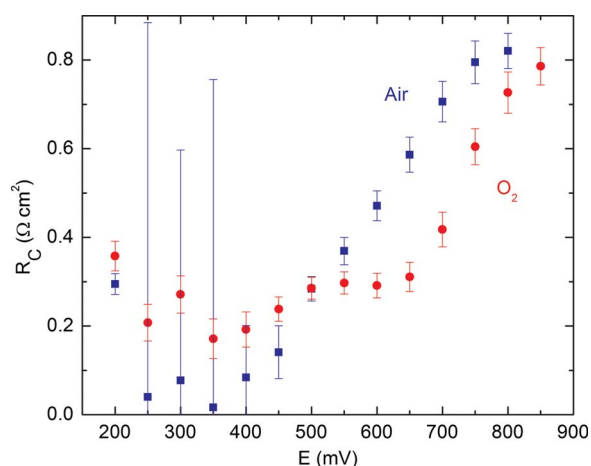


Figure 5. (Color online) Catalyst layer resistance R_C vs potential E obtained from fits to EIS spectra from a Pt/CrN cathode with $w = 0.15 \text{ mg/cm}^2$ Pt operated with air or O_2 .

sumed to be negligible, due to the high electrical conductivity of C, Pt, and CrN. This analysis yields values for charge-transfer resistance R_{CT} , double-layer capacitance C_{DL} , catalyst layer resistance R_C , ohmic resistance R_Ω , and parasitic inductance L . Both data sets exhibit the highest catalyst resistance at high potential, $R_C = 0.79 \text{ } \Omega \text{ cm}^2$ at 0.85 V for O_2 and $R_C = 0.82 \text{ } \Omega \text{ cm}^2$ at 0.80 V for air, and show a decrease in R_C with decreasing E to reach a constant value of $R_C \approx 0.2 \text{ } \Omega \text{ cm}^2$ for $E \leq 0.45 \text{ V}$. The uncertainty in the R_C -values is relatively large for $E \leq 0.35 \text{ V}$, as evident from the scatter in the data and the large error bars plotted in Fig. 5. The error bars are obtained from the fitting procedure and become large when the fit quality is only weakly affected by R_C , which is the case at low potential where the magnitudes of other losses such as mass transport become dominant compared with R_C .

When comparing the data for air and O_2 in Fig. 5, both the minimum and maximum R_C -values at low and high E , respectively, are approximately the same for air and O_2 . We associate the low and high R_C -values with resistance to ionic conduction in a wetted and dry electrode, respectively, consistent with the data presented in Fig. 4. That is, independent of the oxidant, low potential operation leads to water-filled pores that conduct protons from the membrane to active catalyst sites, yielding a low resistance of $\sim 0.2 \text{ } \Omega \text{ cm}^2$. In contrast, operation at high E leads to a drying of the pores and an associated increase in R_C by approximately a factor of 4 to $\sim 0.8 \text{ } \Omega \text{ cm}^2$. Both curves exhibit a relatively steep increase in R_C from 0.3 to $0.8 \text{ } \Omega \text{ cm}^2$, which occurs for air from $E = 0.50$ to 0.75 V , and for O_2 from $E = 0.65$ to 0.85 V . We attribute this effective shift of the air curve by approximately -0.1 V from the O_2 curve to the fact that the gas flow for operation in air is 5 times higher, resulting in a higher water-removal rate from the pores and a correspondingly lower potential (or higher current) for which water removal exceeds water production, yielding a drying of the pores.

The R_C data in Fig. 5 show that the resistance to proton transport is elevated for all $E > 0.5 \text{ V}$ and is the largest at the highest potential. However, the current suppression in the polarization curves in Fig. 3 and 4 is most pronounced for the intermediate potential range of $0.50 \text{ V} < E < 0.75 \text{ V}$, and the curves are nearly unaffected at high potential. This is because the potential drop associated with ionic resistance is proportional to the current. Thus, at high potential low current operation, the current-voltage characteristic is unaffected by the dewetting of the electrode, even if R_C is large, yielding a regular Tafel slope at $E > 0.75 \text{ V}$. As the potential decreases, the current increases and raises the impact of ionic resistance so that b quadruples at an intermediate potential. This is fully consistent with

previous studies, indicating that a 4 times larger slope is expected when the reaction is limited by both proton conduction and oxygen transport.⁵⁹

Conclusion

We have built PEM fuel cell cathode electrodes comprising sputtered Pt layers that are supported by vertically oriented CrN particles grown by GLAD. Their efficiency increases with increasing Pt loading w , but their mass-transport performance during operation in air is nearly independent of w because their porosity and pore size is controlled by the CrN, which is independent of w . Operation with pure O_2 yields anomalous polarization curves, which exhibit a steep $dE/d(\log i)$ in an intermediate potential range of $0.50 \text{ V} < E < 0.75 \text{ V}$ and a shelf at $E \approx 0.5 \text{ V}$, where the current increases substantially. This shelf is attributed to a current-dependent wetting of the catalyst pores that, in turn, controls proton transport. Ramp-rate-dependent measurements as well as EIS spectra indicate that the electrode pores are filled with proton-transporting water during high current ($E < \sim 0.50 \text{ V}$) operation. However, at higher potential, corresponding to a lower current and lower water production rate, the hydrophobic CrN sheds water from the pores so that proton conduction becomes the rate-limiting step. Finally, at the highest potential range, $E > 0.75 \text{ V}$, the ionic conductivity, although relatively low, is sufficient to meet the low proton demand, and the resulting curve follows Tafel kinetics. Scan-rate-dependent polarization curves indicate that the wetting and dewetting processes have approximately the same time constant on the order of 10^3 s , as hysteresis is observed in the polarization curves at scan rates higher than 0.1 mV/s . EIS indicates that within an intermediate potential range, the proton conductivity is the rate-determining step on air as well as O_2 , but for air, mass-transport limitations prevent the cell from accessing the additional catalytic area when the electrode pores fill with water, and no shelf is therefore observed on air operation.

It is concluded that Pt/CrN holds promise as a composite catalyst material. However, proton conductivity is a challenge due to the hydrophobic CrN that limits pore wetting during low current operation. Improved proton conduction may be achieved either by the addition of proton-conducting, hydrophilic ionomer or by decreasing the electrode thickness to maintain a more uniform proton concentration profile, which, however, would introduce additional mass-transport losses or decrease the total surface area, respectively. More generally, the future development of sputter-deposited electrodes requires adequate wetting within the electrode, and the assumption that ultrathin two-phase electrodes are always flooded should be re-examined whenever new materials are introduced.

Acknowledgments

This work was performed within the Center for Fuel Cell and Hydrogen Research at Rensselaer Polytechnic Institute and was supported by the NSF through the IGERT on fuel cells by award no. DGE 0504361 as well as through award no. DMR 0645312 and no. CMMI 0653843.

Rensselaer Polytechnic Institute assisted in meeting the publication costs of this article.

References

1. W. Vielstich, H. A. Gasteiger, and A. Lamm, *Handbook of Fuel Cells: Fundamentals, Technology and Applications*, John Wiley & Sons, New York (2003).
2. S. Litster and G. McLean, *J. Power Sources*, **130**, 61 (2004).
3. M. Uchida, Y. Aoyama, M. Tanabe, N. Yanagihara, N. Eda, and A. Ohta, *J. Electrochem. Soc.*, **142**, 2572 (1995).
4. U. A. Paulus, A. Wokaun, G. G. Scherer, T. J. Schmidt, V. Stamenkovic, N. M. Markovic, and P. N. Ross, *Electrochim. Acta*, **47**, 3787 (2002).
5. M. S. Wilson, F. H. Garzon, K. E. Sickafus, and S. Gottesfeld, *J. Electrochem. Soc.*, **140**, 2872 (1993).
6. J. L. Qiao, M. Saito, K. Hayamizu, and T. Okada, *J. Electrochem. Soc.*, **153**, A967 (2006).
7. H. Tang, Z. G. Qi, M. Ramani, and J. F. Elter, *J. Power Sources*, **158**, 1306 (2006).
8. H. A. Gasteiger, J. E. Panels, and S. G. Yan, *J. Power Sources*, **127**, 162 (2004).
9. E. J. Taylor, E. B. Anderson, and N. R. K. Vilambi, *J. Electrochem. Soc.*, **139**, L45 (1992).
10. H. X. Zhong, X. B. Chen, H. M. Zhang, M. R. Wang, and S. S. Mao, *Appl. Phys.*

- Lett.*, **91**, 163103 (2007).
11. L. Hultman, *Vacuum*, **57**, 1 (2000).
 12. M. F. Weber, S. Mamicheafara, and M. J. Dignam, *J. Electrochem. Soc.*, **134**, 1416 (1987).
 13. D. Gruber and J. Muller, *J. Power Sources*, **171**, 294 (2007).
 14. S. J. Yoo, Y. H. Cho, H. S. Park, J. K. Lee, and Y. E. Sung, *J. Power Sources*, **178**, 547 (2008).
 15. K. L. Huang, Y. C. Lai, and C. H. Tsai, *J. Power Sources*, **156**, 224 (2006).
 16. P. Brault, A. Caillard, A. L. Thomann, J. Mathias, C. Charles, R. W. Boswell, S. Escibano, J. Durand, and T. Sauvage, *J. Phys. D: Appl. Phys.*, **37**, 3419 (2004).
 17. A. T. Haug, R. E. White, J. W. Weidner, W. Huang, S. Shi, T. Stoner, and N. Rana, *J. Electrochem. Soc.*, **149**, A280 (2002).
 18. D. Gruber, N. Ponath, J. Muller, and F. Lindstaedt, *J. Power Sources*, **150**, 67 (2005).
 19. M. D. Gasda, R. Teki, N. Koratkar, T.-M. Lu, G. A. Eisman, and D. Gall, *J. Electrochem. Soc.*, **156**, B614 (2009).
 20. K. Robbie and M. J. Brett, *J. Vac. Sci. Technol. A*, **15**, 1460 (1997).
 21. M. Malac and R. F. Egerton, *J. Vac. Sci. Technol. A*, **19**, 158 (2001).
 22. C. M. Zhou and D. Gall, *Thin Solid Films*, **516**, 433 (2007).
 23. K. Robbie, C. Shafai, and M. J. Brett, *J. Mater. Res.*, **14**, 3158 (1999).
 24. S. Mukherjee, C. M. Zhou, and D. Gall, *J. Appl. Phys.*, **105**, 094318 (2009).
 25. R. Messier, V. C. Venugopal, and P. D. Sunal, *J. Vac. Sci. Technol. A*, **18**, 1538 (2000).
 26. S. V. Kesapragada, P. Victor, O. Nalamasu, and D. Gall, *Nano Lett.*, **6**, 854 (2006).
 27. S. R. Kennedy, M. J. Brett, O. Toader, and S. John, *Nano Lett.*, **2**, 59 (2002).
 28. S. V. Kesapragada, P. R. Sotherland, and D. Gall, *J. Vac. Sci. Technol. B*, **26**, 678 (2008).
 29. S. V. Kesapragada and D. Gall, *Thin Solid Films*, **494**, 234 (2006).
 30. C. M. Zhou and D. Gall, *Small*, **4**, 1351 (2008).
 31. C. M. Zhou, H. F. Li, and D. Gall, *Thin Solid Films*, **517**, 1214 (2008).
 32. C. M. Zhou and D. Gall, *Appl. Phys. Lett.*, **88**, 203117 (2006).
 33. J. Wang, H. C. Huang, S. V. Kesapragada, and D. Gall, *Nano Lett.*, **5**, 2505 (2005).
 34. S. V. Kesapragada and D. Gall, *Appl. Phys. Lett.*, **89**, 203121 (2006).
 35. C. M. Zhou and D. Gall, *J. Appl. Phys.*, **103**, 014307 (2008).
 36. M. D. Gasda, G. A. Eisman, and D. Gall, *J. Electrochem. Soc.*, **157**, B113
 37. B. Dick, M. J. Brett, T. J. Smy, M. R. Freeman, M. Malac, and R. F. Egerton, *J. Vac. Sci. Technol. A*, **18**, 1838 (2000).
 38. R. Nagar, B. R. Mehta, J. P. Singh, D. Jain, V. Ganesan, S. V. Kesapragada, and D. Gall, *J. Vac. Sci. Technol. A*, **26**, 887 (2008).
 39. J. P. Singh, F. Tang, T. Karabacak, T. M. Lu, and G. C. Wang, *J. Vac. Sci. Technol. B*, **22**, 1048 (2004).
 40. Q. P. Wang, M. Eikerling, D. T. Song, and Z. S. Liu, *J. Electrochem. Soc.*, **154**, F95 (2007).
 41. J. Zhang, *PEM Fuel Cell Electrocatalysts and Catalyst Layers: Fundamentals and Applications*, Springer, London (2008).
 42. G. Lin, W. He, and T. Van Nguyen, *J. Electrochem. Soc.*, **151**, A1999 (2004).
 43. V. León, A. Tusa, and Y. C. Araujo, *Colloids Surf., A*, **155**, 131 (1999).
 44. E. Kuze, T. Teramoto, K. Yukimura, and T. Maruyama, *Surf. Coat. Technol.*, **158–159**, 577 (2002).
 45. D.-Y. Wang and M.-C. Chiu, *Surf. Coat. Technol.*, **137**, 164 (2001).
 46. C.-C. Sun, S.-C. Lee, S.-B. Dai, Y.-S. Fu, Y.-C. Wang, and Y.-H. Lee, *Appl. Surf. Sci.*, **252**, 8295 (2006).
 47. *CRC Handbook of Chemistry and Physics*, D. R. Lide, Editor, CRC Press, Boca Raton, FL (2008).
 48. S. Asgharizadeh, M. Sutton, K. Robbie, and T. Brown, *Phys. Rev. B*, **79**, 125405 (2009).
 49. R. Makharia, M. F. Mathias, and D. R. Baker, *J. Electrochem. Soc.*, **152**, A970 (2005).
 50. CrN (03-065-2899), Cr₂N (00-035-0803), and Pt (00-004-0802), in JCPDS International Center for Powder Diffraction Data, Swarthmore, PA.
 51. D. Gall, C. S. Shin, T. Spila, M. Oden, M. J. H. Senna, J. E. Greene, and I. Petrov, *J. Appl. Phys.*, **91**, 3589 (2002).
 52. C. S. Shin, Y. W. Kim, N. Hellgren, D. Gall, I. Petrov, and J. E. Greene, *J. Vac. Sci. Technol. A*, **20**, 2007 (2002).
 53. D. Gall, I. Petrov, N. Hellgren, L. Hultman, J. E. Sundgren, and J. E. Greene, *J. Appl. Phys.*, **84**, 6034 (1998).
 54. T. E. Springer, M. S. Wilson, and S. Gottesfeld, *J. Electrochem. Soc.*, **140**, 3513 (1993).
 55. Q. P. Wang, M. Eikerling, D. T. Song, and Z. S. Liu, *J. Electroanal. Chem.*, **573**, 61 (2004).
 56. N. Agmon, *Chem. Phys. Lett.*, **244**, 456 (1995).
 57. J. Liu and M. Eikerling, *Electrochim. Acta*, **53**, 4435 (2008).
 58. M. Eikerling and A. A. Kornyshev, *J. Electroanal. Chem.*, **475**, 107 (1999).
 59. J. Ihonen, F. Jaouen, G. Lindbergh, A. Lundblad, and G. Sundholm, *J. Electrochem. Soc.*, **149**, A448 (2002).